We are IntechOpen, the world's leading publisher of Open Access books Built by scientists, for scientists

4,800
Open access books available

122,000
International authors and editors

135M
Downloads

Our authors are among the

154
Countries delivered to

TOP 1%
most cited scientists

12.2%
Contributors from top 500 universities

CLARIVATE ANALYTICS BOOK CITATION INDEX INDEXED

WEB OF SCIENCE™

Selection of our books indexed in the Book Citation Index in Web of Science™ Core Collection (BKCI)

Interested in publishing with us?
Contact book.department@intechopen.com

Numbers displayed above are based on latest data collected.
For more information visit www.intechopen.com

Chapter 2

Ion-Exchange Reactions for Two-Dimensional Quantum Antiferromagnetism

Yoshihiro Tsujimoto and Hiroshi Kageyama

Additional information is available at the end of the chapter

http://dx.doi.org/10.5772/52111

1. Introduction

1.1. Insertion of metal halide array

Topotactic low-temperature reactions such as intercalation, deintercalation and ion-exchange reactions provide a rational design of new structures of non-molecular extended solids which are otherwise not accessible by conventional high-temperature solid-state reactions [1-4]. Among candidate oxide materials used as a precursor of such reactions, the most intensively studied system is the Dion-Jacobson (DJ) type layered perovskite (Figure 1). The chemical formula of the DJ phase is expressed as $A'[A_{n-1}B_nO_{3n+1}]$, where A' is an alkali metal (Na, Rb, …), A is an alkaline earth or rare earth metal (Ca, Sr, La, …), B is a d^0 transition metal (Ti, Nb, Ta, …), and n is the number of perovskite layers (2, 3, 4, …) [5, 6]. Here, alkali metal ions at the A' site are highly reactive because of ionic (i.e., weak) A'-O bonding, while the perovskite unit $[A_{n-1}B_nO_{3n+1}]$ is strongly bonded and is chemically inert. By exploiting ion-exchange reactions with various reagents, a wide variety of new or improved chemical and physical functionalities including (photo)catalysis [7, 8], ionic conductivity [9] and superconductivity [10] have been developed. However, ion-exchange reactions are rarely employed for the purpose of materials design toward low-dimensional magnetism, because those who work in this filed (mostly physicists) are not familiar with such chemical processing. In addition, compounds obtained by soft-chemical approaches involve negative effects on the crystal structure, for example, poor crystallinity, non-stoichiometry and defects. In particular, it is known that a tiny defect can easily destroy or mask intrinsic magnetic properties of low-dimensional quantum systems.

In 1999, John B. Wiley *et al*. in the University of New Orleans reported a new type of ion-exchange reactions involving the simultaneous co-exchange of transition-metal cation and chloride anion [11]. As shown in Figure 1(a) and 1(b), the reactions of the n = 2 and 3 DJ

phases using CuX_2 (X = Cl, Br) result in the Rb^+-to-$(CuX)^+$ exchange, yielding new metastable compounds $(CuX)^+[A_{n-1}B_nO_{3n+1}]^-$ [11, 12]. Here, the Cu^{2+} ions are octahedrally coordinated, bridging between two apical oxide ions from the perovskite blocks and also surrounded by four halogen ions. The CuO_2X_4 octahedra share edges to form a square lattice network in the *ab* plane. $(CuX)A_{n-1}B_nO_{3n+1}$ has two interesting features in terms of magnetic interactions. First, the chemical bonds between the transition-metal cations and halide anions are covalent, thereby providing sizable Cu-*X*-Cu superexchange interactions within the Cu*X* layer. Second, the two-dimensional (2D) Cu*X* layers are well-separated by the non-magnetic perovskite blocks $A_{n-1}B_nO_{3n+1}$ along the *c*-axis, with the interlayer distance of 12 Å (n = 2) and 16 Å (n = 3). Thus, $(CuX)A_{n-1}B_nO_{3n+1}$ is regarded as an ideal candidate of S = 1/2 2D square lattice systems (Figure 1(c)). What is also important is the fact that this ion-exchange reaction proceeds stoichiometrically, making it possible in principle to observe intrinsic quantum phenomena.

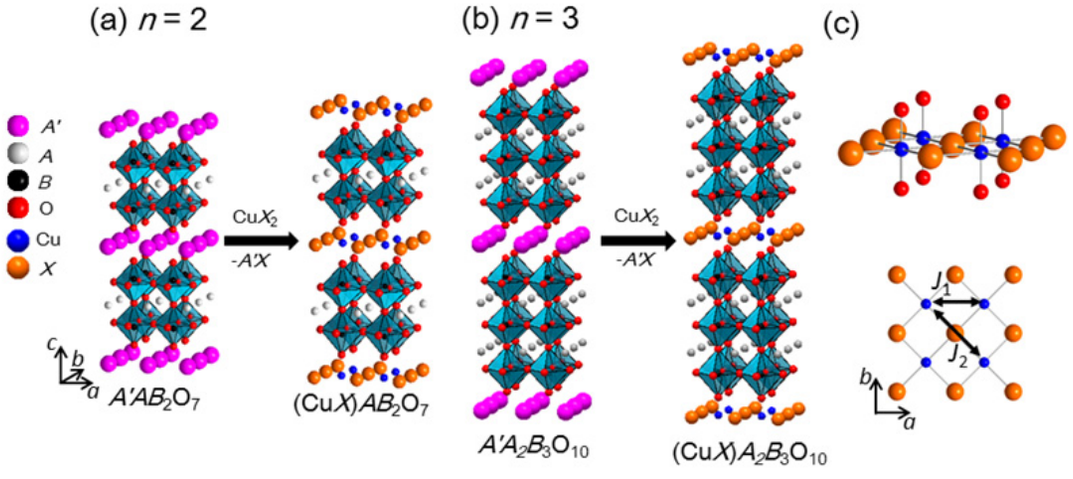

Figure 1. Ion-exchange reaction involving the insertion of copper halide layer into the interlayer spaces of the Dion-Jacobson type layered perovskites $A'[A_{n-1}B_nO_{3n+1}]$ for (a) n = 2 and (b) n = 3. (c) Local coordination environment around the copper atom. J_1 and J_2 denote nearest-neighbor and 2nd nearest-neighbor exchange constants, respectively.

1.2. A new family of two-dimensional quantum antiferromagets

A simple geometrical consideration reveals that the magnetism of $(CuX)A_{n-1}B_nO_{3n+1}$ is described by a square-lattice J_1-J_2 model, where J_1 and J_2 represent the nearest neighbor (NN) interaction and the 2nd NN interaction (Figure 1(c)). According to the Goodenough-Kanamori rule, J_1 and J_2 are expected to be ferromagnetic (FM) and antiferromagnetic (AFM), respectively, giving a situation where geometrical frustration is present in the lattice. The J_1-J_2 model was originally proposed to explain the origin of high-T_c superconductivity in carrier-doped cuprates with S = 1/2 square lattice [13]. Although the detail of theoretical phase diagram is still controversial [14-18], regardless of the approaches employed, several interesting phases appear as a function of $\alpha = J_2/J_1$ (see Figure 2). Let us define hereafter positive and negative J as AFM and FM interaction, respectively. The most interesting phase

predicted is a spin liquid phase with a spin-singlet ground state, being located at around $\alpha \sim |0.5|$ (in the regions of both $J_1 < 0$, $J_2 > 0$ and J_1, $J_2 > 0$), where frustration effect is most prominent. So far, several prototypes of the J_1-J_2 model were reported, for example, $Li_2VO(Si,Ge)O_4$ [19] and $Pb_2VO(PO_4)_2$ [20]. Unfortunately, all of them undergo magnetic long-range ordering at low temperatures and the estimated α values are far from $\alpha \sim |0.5|$. In contrast, the magnetic study for $(CuCl)LaNb_2O_7$ revealed that this material does not show long-range magnetic order down to low temperatures [21]. $(CuCl)LaNb_2O_7$ and related compounds obtained by ion-exchange process exhibit a rich variety of quantum phenomena due to geometrical frustration. Hereafter, we will overview recent studies of the ion-exchanged $(CuX)A_{n-1}B_nO_{3n+1}$ compounds, which allows a systematic understanding and tuning of magnetic properties.

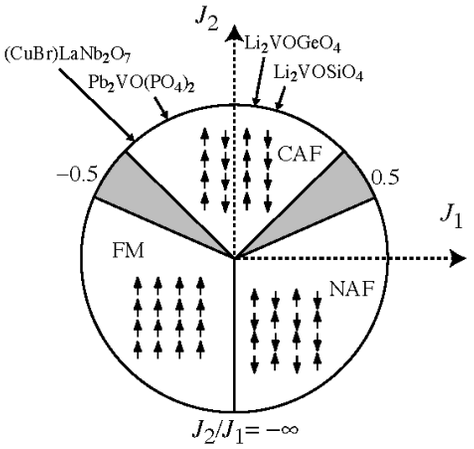

Figure 2. Phase diagram of the J_1-J_2 model on the square lattice where FM, NAF, CAF represent a (0 0) ferromagnetic state, a (π π) Néel antiferromagnetic state, and a (π 0) collinear antiferromagnetic state.

2. Crystal structures and magnetic properties

2.1. Double layered system

2.1.1. (CuCl)LaNb$_2$O$_7$

A polycrystalline sample of $(CuCl)LaNb_2O_7$ is typically synthesized by heating a mixture of $RbLaNb_2O_7$ and anhydrous $CuCl_2$ at 320 °C for 1 weak. The white specimen becomes light green after the ion-exchange reaction. This color change is due to insertion of Cu^{2+}. The crystal structure of $(CuCl)LaNb_2O_7$ was originally assigned as tetragonal (space group *P*4/*mmm*), with one copper ion at (1/2, 1/2, 1/2) and one chlorine ion at (0, 0, 1/2) per unit cell, forming the ideal S = 1/2 square lattice. Shortly later, the neutron powder diffraction suggested the same space group but a random distribution of chlorine atoms at more general site (x, 0, 1/2) [22]. The tetragonal lattice constants are a = 3.88 Å, c = 11.73 Å. Compared with $RbLaNb_2O_7$ (a = 3.90 Å, c = 11.03 Å), the c-axis of the ion-exchanged product significantly increases by ~ 0.7 Å, while the a-axis remains almost unchanged. This is consistent with cupper occupation between two terminal apical oxide ions from NbO_6 octahedra.

The absence of long-range magnetic order in (CuCl)$LaNb_2O_7$ down to low temperatures was demonstrated first by means of magnetic susceptibility and inelastic neutron scattering (INS) experiments [21]. On cooling, the magnetic susceptibility χ (= M/T) (Figure 3) exhibits a Curie-Weiss (CW) behavior followed by a broad peak at around 16.5 K, which is characteristic of low-dimensional AFM system. The χ decreases rapidly with decreasing temperature further. The Weiss temperature θ estimated from the CW fitting is –9.6 K. The magnitude of θ is smaller than the temperature at the broad maximum, indicating the presence of competing FM and AFM interactions. The obtained value of C (= 0.385 emu K/mol) agrees well with that expected theoretically for 1 mol of Cu^{2+}, ensuring (almost) completion of the ion-exchange reaction. The upturn at 3.5 K in the raw data is ascribed to a tiny amount of Cu-containing impurities or defects in the CuCl layers. When the impurity contribution was subtracted, the intrinsic susceptibility approaches to zero for $T \to 0$. As shown in Figure 4(a), the INS measurements (constant-Q scan in zero field), carried out at JRR-3, Tokai, Japan, provide direct evidence for the spin-singlet ground state with a one-triplet excitation gap of Δ = 2.3 meV. The full widths at half maximum (FWHM) for the 2.3 meV excitation is 1.3 meV, being close to the instrumental resolution. The scattering intensity of the one-triplet excitation decreases with increasing T and levels off above approximately 20 K, a temperature comparable to the spin gap. There is another excitation centered at 5.0 meV, whose T-dependence shows the same tendency as that of the one-triplet transition. Accordingly, the second mode is the collective bound state excitations of several elementary triplets.

In general, magnetic excitations in 2D systems with a spin-singlet ground state are highly dispersive along the magnetic plane. However, the spectrum shape in constant Q scans for the one-triplet mode in powder (CuCl)$LaNb_2O_7$ specimen is completely symmetric and almost independent of Q (ΔE ~ 0.2 meV), indicating an extremely localized nature of the excited triplets. Such a flat dispersion is characteristic of isolated spin dimer systems such as $CaCuGe_2O_6$ [23]. Since the Cu spins in (CuCl)$LaNb_2O_7$ are not isolated, the observation of the dispersionless spin spectrum is a consequence of geometrical frustration. The same behavior has been observed in the 2D Shastry-Sutherland system $SrCu_2(BO_3)_2$, where compared to in-plane exchange constants (5 – 8 meV) the dispersion of the single-triplet excitation is much suppressed (~ 0.02 meV) [24]. As shown in Figure 4(b), the Q dependence of the scattering intensity of the singlet-triplet excitation, I(1.7 K) – I(20 K), exhibits a fast oscillation. The geometrical frustration in (CuCl)$LaNb_2O_7$ gives a situation that the spin-singlet pairs are *effectively* isolated, which may allow us to use the isolated dimer model:

$$I(Q) \propto F^2(Q)\left(1-\frac{\sin QR}{QR}\right) \tag{1}$$

where the second term $\sin QR/(QR)$ is the interference term reflecting the intradimer distance R. Unexpectedly, the estimated value of R is 8.8 Å, which is far longer than the NN Cu-Cu distance (~ 3.9 Å), and is rather close to the 4th NN distance (8.67 Å). This result contradicts the J_1-J_2 model, where the NN bonds are responsible for the spin-singlet formation.

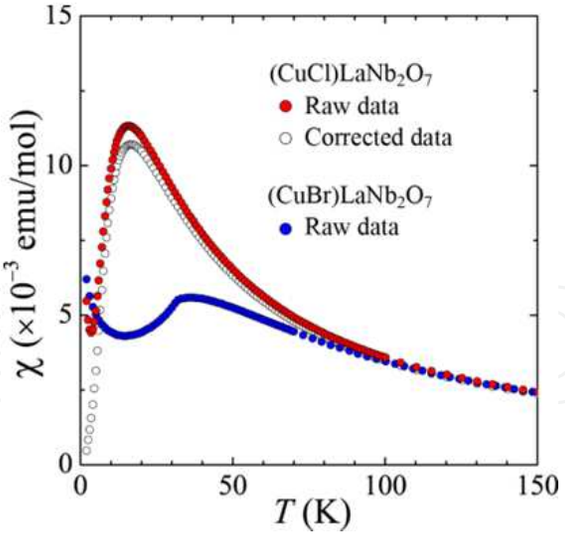

Figure 3. Temperature dependence of the magnetic susceptibility in (Cu*X*)$LaNb_2O_7$ (*X* = Cl, Br) [21, 37].

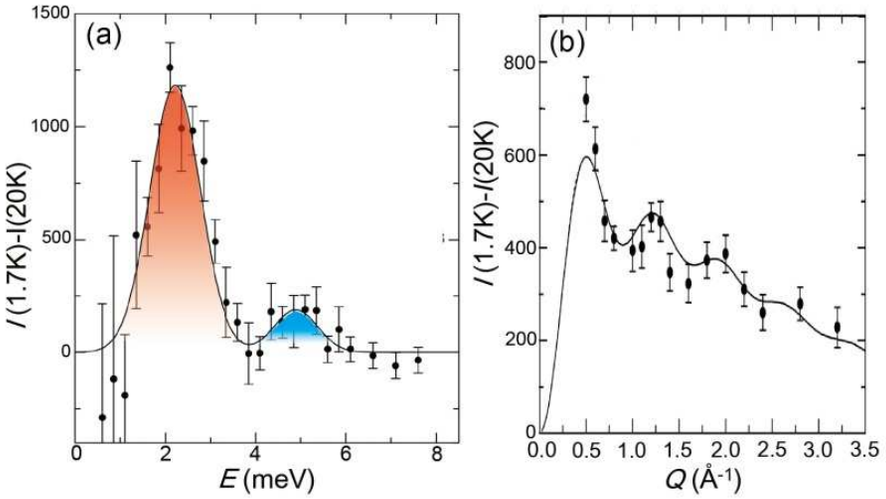

Figure 4. (a) Constant-*Q* scan at 0.8 Å^{-1} in (CuCl)$LaNb_2O_7$. The solid circles are the difference, *I*(1.7 K) – *I*(20 K) [21]. (b) The *Q* dependence of the transition at 2.3 meV. The solid line indicates the fit according to eq. (1), which resulted in *R* = 8.8 Å [21].

Figure 5 shows the field dependence of magnetization *M*-*H* and the differential magnetization d*M*/d*H* at 1.3 K [25], demonstrating field-induced phase transitions at H_{c1} = 10.3 T and H_{c2} = 30.1 T. Reflecting the spin-singlet ground state with a finite energy gap, the initial magnetization slope is very small. Note that the small increase for $H < H_{c1}$ comes from a tiny amount of impurities or defects as also seen in the magnetic susceptibility for $T < 5$ K. The intrinsic magnetization curve is obtained by subtracting the extrinsic component (2.0% of free magnetic ions of $S = 1/2$) from the raw magnetization. The field-induced transition at H_{c1} should be caused by the level crossing of the singlet and one of triplet states, following the relation $H_{c1} = \Delta/g\mu_B$, where Δ is the gap in zero field. However, the observed value of H_{c1} is much smaller than 18.5 T calculated from the neutron data (Δ = 2.3 meV). This observation indicates that some other states like a two-triplet bound state causes the level crossing at H_{c1}.

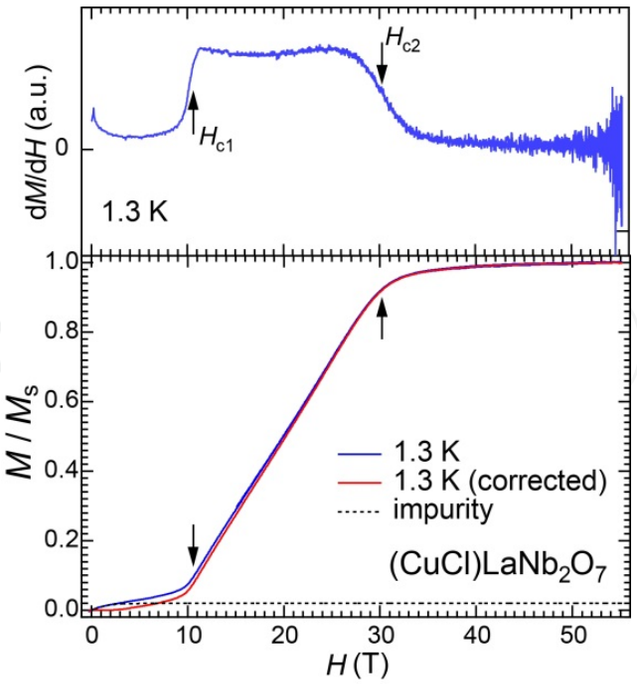

Figure 5. Magnetization curve measured at T = 1.3 K and its derivative [25]. Arrows point to the transition fields.

For $H_{c1} < H$, the magnetization gradually increases up to the saturated magnetization. This intermediate state is stable over a wide field range ($H_{c2} - H_{c1}$ = 19.8 T), which is due to substantial interdimer interactions. No magnetization plateaus are observed, unlike $SrCu_2(BO_3)_2$ with 1/8, 1/4, and 1/3 plateaus [26, 27] and NH_4CuCl_3 with 1/4 and 3/4 plateaus [28]. Such a difference is understood in terms of competition between localization and delocalization among excited triplets. The magnetization is correlated with the total number of magnons N through the relation $M = g\mu_B N$. The chemical potential of the $S^z = +1$ magnons is described as $\mu = g\mu_B(H - H_{c1})$. The transverse components of the exchange interactions generate hopping of the magnons, while the longitudinal components generate repulsion of the magnons. When the delocalization term is dominant as in the present material, the Bose-Einstein condensation (BEC) of excited triplets, or magnons, occurs. On the other hand, when the localization term is dominant, magnons are crystallized in an ordered fashion to minimize the repulsive interactions, leading to a plateau in the magnetization curve.

Figure 6(a) shows the temperature dependence of total specific heat C_P (in the inset) and C_P/T under applied magnetic fields ranging from 0 to 14 T [29]. The zero field data reveal no anomaly associated with a long-range magnetic ordering, in consistent with magnetic susceptibility and INS experiments. The Schottky anomaly is seen at around 7 K. After subtracting the lattice contribution βT^3 (β = 0.717 mJ/K^4 mol), the magnetic contribution C_m is obtained, and the subsequent T-integration of C_m/T gives the magnetic entropy S_m of 1.1 J/mol K, which is 13% smaller than the total magnetic entropy (Rln2) for 1mol of S = 1/2.

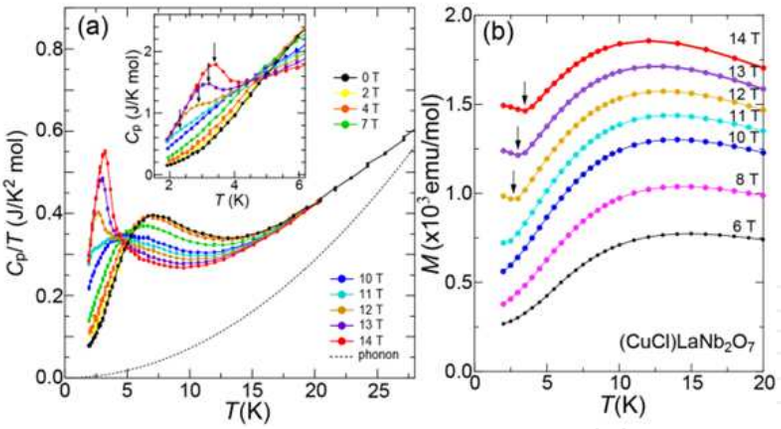

Figure 6. (a) C_P/T for (CuCl)$LaNb_2O_7$ collected under several fields. The dotted curve represents the phonon contribution βT^3. The inset shows the C_P vs T plots. Arrows denote the transition temperature [29]. (b) Low-temperature magnetizations measured at various external magnetic fields up to 14 T [29].

When the magnetic field is increased up to 7 T, the broad maximum of C_P/T shifts gradually to lower temperature, indicating reduction of the spin gap owing to Zeeman splitting of the excited triplet states (Figure 6(a)). The broad maximum in $C_P(T)/T$ changes into a cusp at and above 11 T (H_{c1}), corresponding to the field-induced transition to the BEC state. When the magnetic field is further increased, the peak associated with the phase transition develops and shifts systematically to higher temperatures. The transition temperatures T_N at 11 T and 14 T are 2.3 K and 3.3 K, respectively. The growth of the peak area at T_N is consistent with the BEC scenario. Figure 6(b) shows the temperature dependence of magnetization at various constant magnetic fields. A cusp-like anomaly above 10 T shows the occurrence of the BEC transition. The increase in magnetization with decreasing temperature below T_N corresponds to the increased magnon density on the basis of the BEC scenario. Shown in Figure 7 is a T vs H phase diagram. All $C_P(T)$, $M(T)$ and $M(H)$ data agree well with one another. A theoretical curve based on the Hartree-Fock approximation gives the power low behavior $[H_c(T) - H_c(0)] \propto T^{\phi}$ with the critical exponent $\phi = 3/2$ [30].

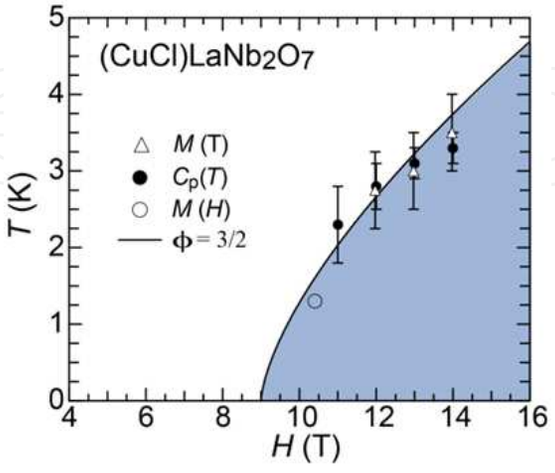

Figure 7. Phase boundary between spin-singlet state and the BEC state in (CuCl)$LaNb_2O_7$ determined from the results of $M(T)$, $M(H)$, and $C_P(T)$. The solid line represents a theoretical curve described in the text [29].

Nuclear magnetic resonance (NMR) is a useful tool to clarify the local symmetry. It is revealed that none of the Cu, Cl, and La sites have the tetragonal symmetry [31], which is incompatible with the initially reported tetragonal structure with *P*4/*mmm* [11]. For example, the Cu- and Cl-NMR spectra could not be accounted for by C_4 symmetry along the *c* direction. Furthermore, transmission electron microscopy (TEM) measurements demonstrated superlattice reflections indicating the doubling along *a*- and *b*-axes ($2a \times 2b$). From the obtained spectra, a single-site occupation without site disorder is indicated for both Cu and Cl, in contradiction to the early neutron diffraction study [22]. In addition, the Nb hyperfine coupling constant for $H \parallel c$ is as large as 2.84(8) T/μ_B, suggesting a strong Cu-O-Nb hybridization. Thus, the in-plane magnetic interactions come not only by the Cu-Cl-Cl superexchange pathways but also by the Cu-O-O-Cu super-superexchange pathways. Figure 8 shows two possible superstructures of the CuCl layer, proposed on the basis of the NMR and TEM results [31].

A single crystal X-ray diffraction is essential to determine the *real* crystal structure. However, the difficulty is that one cannot directly obtain the single crystal of $(CuCl)LaNb_2O_7$ by a conventional high-temperature flux method, because it is a metastable phase. Nevertheless, the $(CuCl)LaNb_2O_7$ single crystals could be obtained topochemically through the ion-exchange reaction of the $CsLaNb_2O_7$ single crystals [32, 33]. The $CsLaNb_2O_7$ crystal was grown by a self-flux method [34]. As shown in Figure 9, transparent, plate-shaped crystals with a typical size of $0.5 \times 0.5 \times 0.1$ mm^3 are obtained. The crystals of $CsLaNb_2O_7$ were embedded in $CuCl_2$ powder, for the ion exchange at 340 °C for 1 week. This yielded dark-green single crystals of $(CuCl)LaNb_2O_7$. Energy dispersive spectroscopy (EDS) shows the absence of Cs in the crystal after the reaction. The time-dependent study revealed that, despite the use of large single crystal and low temperature for reaction, the diffusion occurs surprisingly fast, at a rate of 20 μm h^{-1}.

The crystal structure of $(CuCl)LaNb_2O_7$ was refined using single crystal X-ray diffraction and high- resolution powder neutron diffraction data, and Figure 9(b) shows the determined structure [32]. $(CuCl)LaNb_2O_7$ adopts the orthorhombic $2a \times 2b \times c$ superstructure with the *Pbam* space group. The lattice constants at 2 K are a = 7.7556 Å, b = 7.7507(5) Å, and c = 11.7142(4) Å. The closeness of the in-plane constants is the reason why earlier low-resolution X-ray/neutron studies gave a tetragonal cell. In the new structure, the NbO_6 octahedra are strongly tilted around the *a*-axis in a staggered manner. The tilting pattern of the NbO_6 is correlated with the positions of both the Cu and Cl atoms. In particular, the Cl atoms move significantly along the *b* direction and slightly along *a* direction from their tetragonal position. The Cu ions occupy the 4*h* site are displaced along the *a*- and *b*-axis, yielding different Cu-Cu distances of 3.626 Å and 4.129 Å along the *b*-axis and 3.885 Å along the *a*-axis. The Cu ions take octahedral coordination against two oxide ions with a distance of 1.865 Å and against four chlorine ions with two shorter bonds (2.386 Å and 2.389 Å) and two longer bonds (3.136 Å and 3.188 Å). When the local *z* and *x* axes for each Cu^{2+} are taken along the Cu-O and the short Cu-Cl bonds, respectively, the overall symmetry of the magnetic orbital including the ligand *p* orbitals has the z^2–x^2 character, making the exchange interactions in the CuCl layer highly anisotropic.

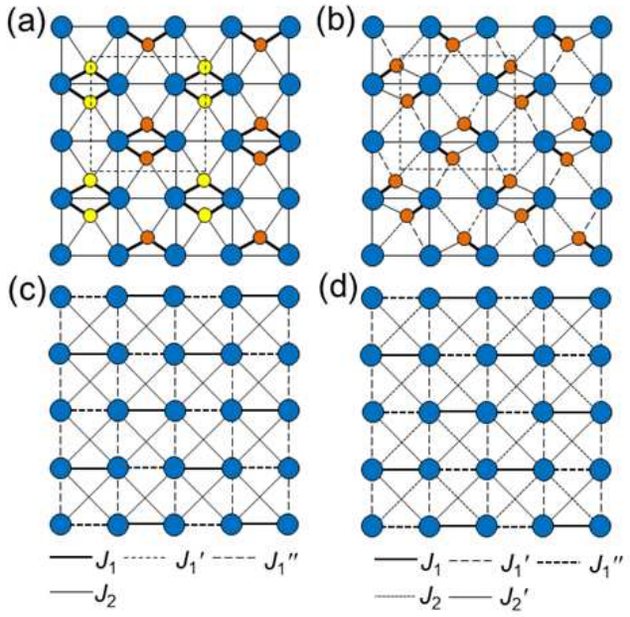

Figure 8. (a, b) Superstructures and (c, d) their corresponding exchange paths for the CuCl layer, suggested by NMR/NQR and TEM experiments. The yellow/orange and blue circles represent the Cl and Cu ions, respectively [31]. The dashed lines in (a) and (b) indicate the unit cell for the superstructure. In the structure (a), the yellow and orange circles represent Cl atoms above and below the Cu layer, respectively.

The first principles calculations based on the new structure [32] yielded the superexchange interactions (see Figure 10(a) and Table 1). Interestingly, the 4th NN interaction, J_4, of the Cu-Cl-Cl-Cu exchange path is the strongest and is AFM. The other 4th NN interaction, J_4' is also AFM, but is much weaker than J_4 ($J_4'/J_4 = 0.18$). This is understood as J_4 has a larger Cu-Cl-Cl angle and a shorter Cl-Cl distance than J_4' (164.9° and 3.835 Å for J_4 vs 156.0° and 4.231 Å for J_4'). The other major J's are FM. The relative strength of the six exchange interactions is $J_4 > J_{1a} > J_{2a} > J_4' > J_{2b} > J_{1b}$.

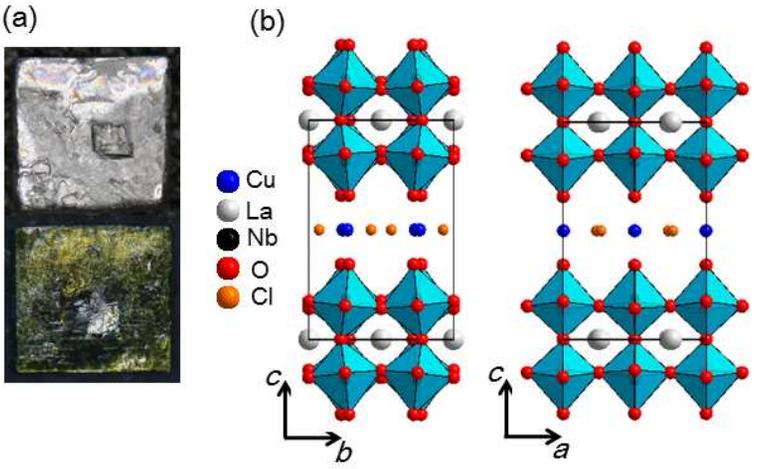

Figure 9. (a) Photos of single crystals of $CsLaNb_2O_7$ (top) and ion-exchanged $(CuCl)LaNb_2O_7$ (bottom) [33]. (b) Projection of the crystal structure for [100] (left) and for [010] (right) [32].

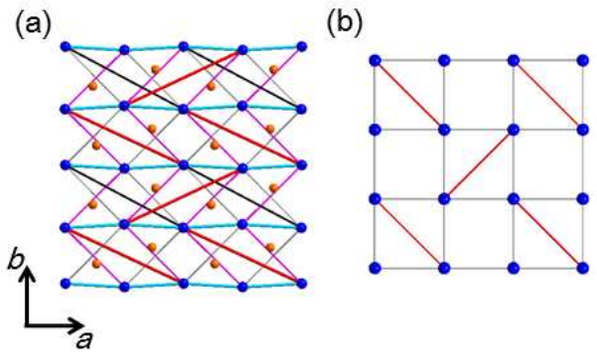

Figure 10. (a) Exchange interactions in the CuCl layer in (CuCl)$LaNb_2O_7$ based on the revised structural model. The lines connecting Cu atoms represent exchange interactions: J_{1a} (light blue), J_{2a} (pink), J_{2b} (gray), J_4 (red), and J_4' (black). J_{1b} is not plotted for clarity [32]. (b) Shastry-Sutherland model where spin dimers form the orthogonal array [35].

J_s	path	d (Å)	angle (°)	J_s/J_4
J_{1a}	Cu-Cl-Cu	3.88548	108.9, 75.8	–0.39
J_{1b}	Cu-Cl-Cu	3.88548	80.9	–0.04
J_{2a}	Cu-Cl-Cu	5.46148	156.7	–0.38
J_{2b}	Cu-Cl-Cu	5.5053	170.2	–0.14
J_4	Cu-Cl-Cl-Cu	8.81262	164.9	1
J_4'	Cu-Cl-Cl-Cu	8.53250	150.0	0.18

Table 1. Exchange paths for up to the fourth NN interactions in (CuCl)$LaNb_2O_7$ and the corresponding coupling constants relative to the strongest AFM interaction J_4 [32].

The strongest AFM J_4 gives the spin-singlet dimers in (CuCl)$LaNb_2O_7$. The distance of Cu-Cl-Cl-Cu (J_4 bond) is 8.533 Å, which is in good agreement with the intradimer distance obtained from the INS analysis (Figure 4b). Using the set of J values, the INS data was analyzed again and the better agreement was obtained [32]. Most remarkably, the 4th NN Cu ions form spin singlet arranged in a staggered manner in the *ab* plane (Figure 10a) and the coupling between them is primarily ferromagnetic. Therefore, the spin lattice is best described as ferromagnetically coupled Shastry-Sutherland quantum spin singlet [32, 35]. In otehr words, (CuCl)$LaNb_2O_7$ is a ferromagnetic counterpart of $SrCu_2(BO_3)_2$.

2.1.2. (CuBr)$LaNb_2O_7$

(CuBr)$LaNb_2O_7$ is synthesized in a way similar to (CuCl)$LaNb_2O_7$, but using $CuBr_2$ [11]. The color of the cupric bromide is brown. The structure of (CuBr)$LaNb_2O_7$ has the tetragonal $P4/mmm$ space group (a = 3.90 Å and c = 11.70 Å), without any superstructure. When this structure is assumed when refined, the Br atoms exhibits an extraordinarily large displacement parameter U_{iso} = 0.087 Å^2. As in the case of (CuCl)$LaNb_2O_7$, a deviation from the tetragonal $P4/mmm$ structure is inferred from the NMR/NQR experiments [36]. The Cl-to-Br replacement resulted in the magnetic order. Figure 3 shows $\chi(T)$ of this

material [37]. The CW fitting gives $\theta = -5.1$ K. The $\chi(T)$ shows a round maximum at T_{max} = 36 K, which is much larger than θ in magnitude, suggesting competing AFM and FM interactions. A tiny kink is seen at 30 K, right below T_{max}, which is ascribed to magnetic order. Consistently, the specific heat measurements show a peak at 32 K. The neutron diffraction experiments demonstrated a collinear antiferromagnetic (CAF) order with a modulation vector of (1/2 0 1/2). The estimated magnetic moment is 0.60(11) μ_B. The reduced magnetic moment probably results from quantum fluctuations. Figure 11 shows the high-field magnetization $M(H)$ measured at 1.3 K. For $0 < H < 30$ T, $M(H)$ increases linearly with magnetic fields, which is followed by non-linear growth. The upward curvature should be caused by the gradual suppression of zero-point oscillations by the external field and is expected to be observed in the framework of spin-wave theory. On the assumption of the J_1-J_2 model [17], J_1/k_B and J_2/k_B are estimated as –35.6 K and 41.3 K, giving $\alpha = |J_2/J_1| = 1.10$, which is located within the range of the CAF phase in the J_1-J_2 model (Figure 2).

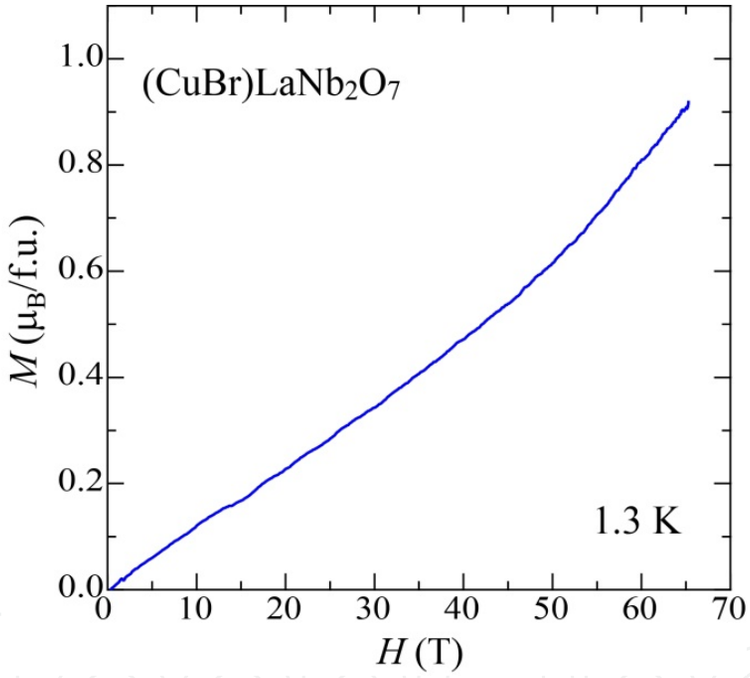

Figure 11. High-field magnetization for $(CuBr)LaNb_2O_7$ at 1.3 K [37].

2.1.3. Cu(Cl, Br)La(Nb, Ta)$_2$O$_7$

Two kinds of solid solutions have been investigated, against Br-for-Cl [38, 39] and Ta-for-Nb [39, 40] substitution. For $(CuCl_{1-x}Br_x)LaNb_2O_7$ ($0 \le x \le 1$), the a-axis linearly increases with x, while the c-axis decreases. The temperature dependence of the magnetic susceptibility (Figure 12(a)) shows the reduction of Néel temperature from T_N =32 K (x = 1), 25 K (x = 0.67), 21 K (x = 0.5), 17 K (x = 0.33) (Figure 12(b)). The magnetization curves for $x \ge 0.33$ show a linear increase over a wide field range, and the saturation field decreases with decreasing the Br concentrations, implying a weaker superexchange constant for Cu-Cl-Cu than Cu-Br-Cu.

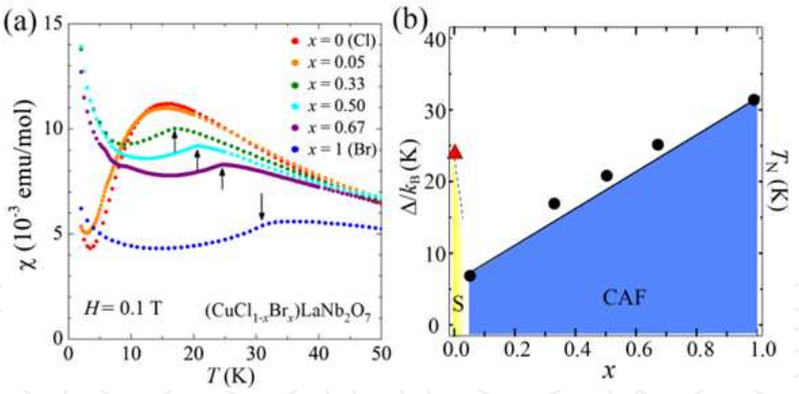

Figure 12. (a) Magnetic susceptibilities of $(CuCl_{1-x}Br_x)LaNb_2O_7$ [38]. (b) x dependence of T_N. S and CAF stand for the spin-singlet state and the collinear antiferromagnetic state [38].

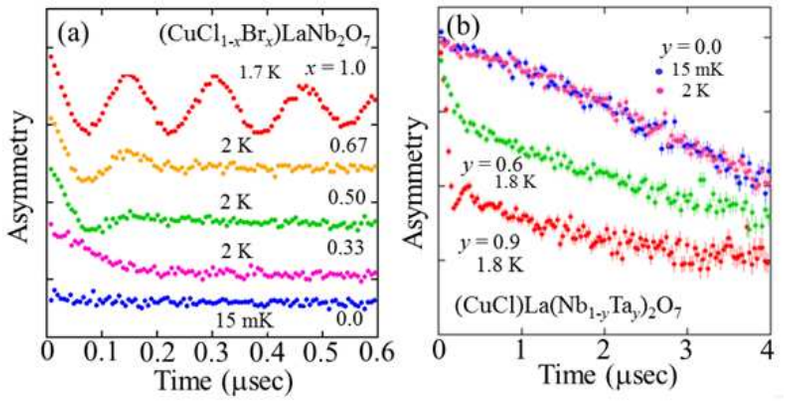

Figure 13. ZF-μSR time spectra in $(CuCl_{1-x}Br_x)LaNb_2O_7$ and $(CuCl)La(Nb_{1-y}Ta_y)_2O_7$ [39].

Muon spin relaxation (μSR) offers a unique opportunity in detecting a static magnetic order at high sensitivity. Figure 13 shows the Zero-field (ZF) μSR spectra of $(CuCl_{1-x}Br_x)LaNb_2O_7$ [39]. The x = 1 spectrum exhibits a long-lived precession below T_N, indicating the existence of a well-defined local field at the muon site expected for homogeneous long-range order. With decreasing x, the internal field at ~ 2 K becomes increasingly inhomogeneous as shown by the damping of the oscillation. The x = 0.05 also exhibits a long-range magnetic order at 7 K, in spite of the spin–gapped behavior in magnetic susceptibility and magnetization. The inhomogeneous static local field was observed in the low x range, a characteristic behavior often seen in dilute alloy spin-glass systems [41]. The change in the initial damping rate between x = 0.33 and 0.05 indicates that the size and/or spatial uniformity of the ordered moment changes between these two Br concentrations. In fact, the neutron scattering experiments for x = 0.05 reveals the CAF ordered structure with a magnetic moment being significantly reduced to 0.2(1) μ_B. The long-range magnetic order induced by only 5%-Br doping and the significantly reduced ordered moment indicates that $(CuCl)LaNb_2O_7$ is located in the vicinity of the quantum phase boundary adjacent to the ordered state.

Contrasting behaviors are observed in the Nb-site substituted system, $(CuCl)La(Nb_{1-y}Ta_y)_2O_7$ ($0 \le y \le 1$) [40]. Reflecting similar ionic radii between Nb^{5+} and Ta^{5+}, the lattice parameters are almost constant with y. However, the magnetic ground state is affected significantly by the

Nb-to-Ta substitution. The magnetic susceptibility of (CuCl)$LaTa_2O_7$ exhibits a broad maximum at T_{max} = 11.5 K, which is close to 16.5 K in (CuCl)$LaNb_2O_7$. However, it exhibits only a slight decrease below T_{max}, indicating a magnetic ground state. The neutron diffraction and μSR experiments (Figure 13(b)) evidence a magnetic order at 7 K, with the reduced magnetic moment of 0.69(1) μ_B and the propagation vector of (1/2 0 1/2). Unlike the (Cl, Br) solid solution, the spin-singlet state is quite robust against the Ta substitution. Substantial substitution up to y ~ 0.4 is necessary to induce the magnetic order. It is remarkable that the spin disordered phase persists up to y = 0.9. This indicates the occurrence of the phase separation. In this range, T_N remains almost unchanged against the Ta concentrations (Figure 14). The volume fraction of the spin-disordered phase increases with decreasing y. It should be noted that the observed phase separation is not caused by chemical inhomogeneity because of uniform distribution of the Nb and Ta atoms as revealed by TEM/EDS images.

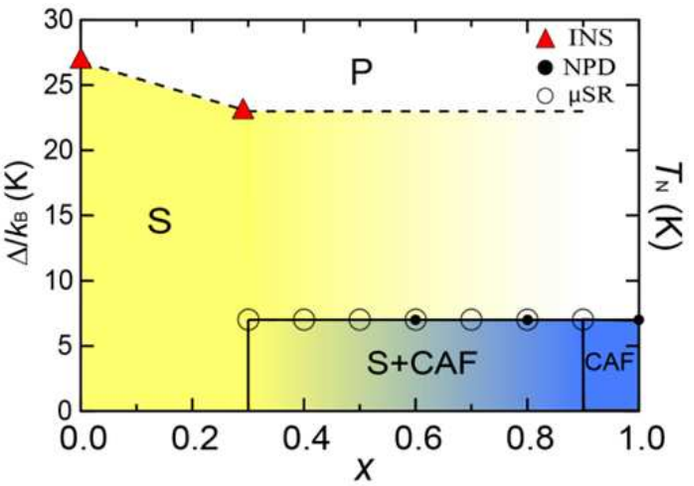

Figure 14. Magnetic phase diagram as a function of temperature and concentration. P, S and CAF stand for the paramagnetic state, the spin-singlet state, and the collinear type AFM state, respectively [40].

The difference in magnetic behaviors between *A*- and *B*-site solid solutions is accounted for by the chemical randomness; the superexchange interactions mediated by halogen atoms should be larger than those mediated the non-magnetic perovskite block. Some theories on 1D systems showed the staggered spin-spin correlations in the vicinity of spin vacancies, which results in the emergence of the ordered phase as observed in $CuGeO_3$ [42] and $SrCu_2O_3$ [43]. By analogy, the induced magnetic order by a small amount of Br substitution in (CuCl)$LaNb_2O_7$ may be associated with staggered correlations induced around Br ions.

2.2. Triple layered system

2.2.1. (CuBr)$Sr_2Nb_3O_{10}$

(CuBr)$Sr_2Nb_3O_{10}$ is a triple-layered compound, prepared by the ion-exchange reaction of $RbSr_2Nb_3O_{10}$ with $CuBr_2$ at 350 °C for 1 week. The crystal structure of (CuBr)$Sr_2Nb_3O_{10}$ at room temperature is tetragonal (a = 3.91069(4) Å, c = 16.0207(3) Å) with the space group

*P*4/*mmm* [44, 45]. As in the double layer compounds, a random displacement of the Br atoms from the ideal site is pointed out. In comparison with the double-layered system, the *c* axis is expanded by ~ 4 Å corresponding to the one-perovskite unit. Thus, the enhanced two-dimensionality is expected in magnetism.

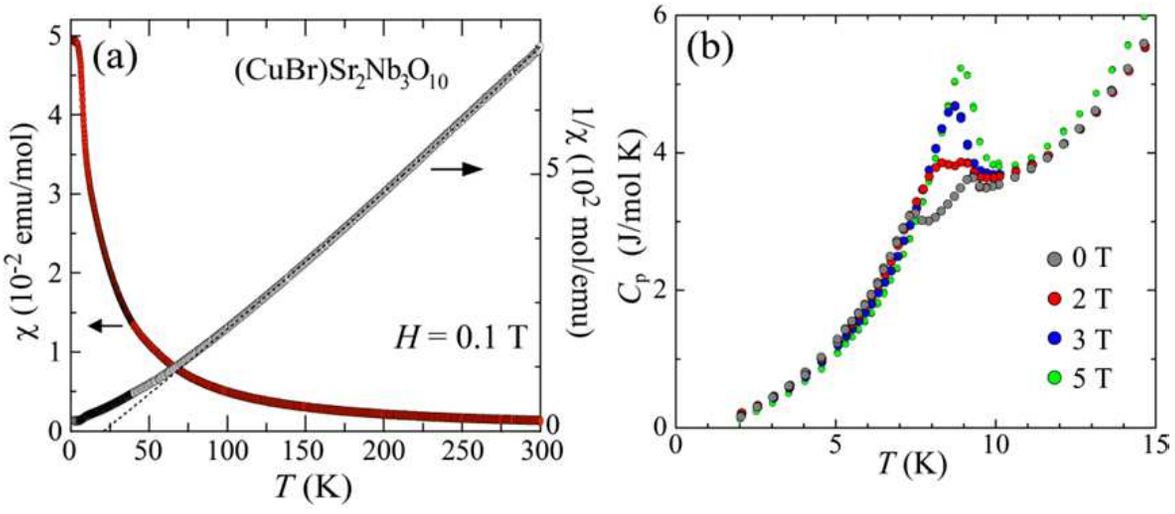

Figure 15. (a) Temperature dependence of the (inverse) magnetic susceptibility for $(CuBr)Sr_2Nb_3O_{10}$ measured at 0.1 T [44]. (b) C_p vs T measured at 0, 2, 3, and 5 T [44].

Figure 15(a) shows the temperature dependence of the magnetic susceptibility for $(CuBr)Sr_2Nb_3O_{10}$ measured at H = 0.1 T. The CW fitting gives θ = 20.9(3) K. The positive θ implies that FM interactions are dominant over the AFM ones, which is in contrast to the negative θ for the double layered compounds: –9.6 K for $(CuCl)LaNb_2O_7$ [21] and –5.1 K for $(CuBr)LaNb_2O_7$ [37]. Instead of a broad maximum in $\chi(T)$ typically seen for low-dimensional spin systems, $\chi(T)$ increases with reducing T until it flattens out below 5 K. A noticeable anomaly associated with a long-range magnetic order is not seen. However, specific heat measurements in Figure 15(b) show successive phase transitions at 9.3 K (T_{c1}) and 7.5 K (T_{c2}). Non-discontinuous character and the absence of T hysteresis in $C_p(T)$ as well as $\chi(T)$ indicate the 2nd-order phase transitions. Successive phase transitions are characteristic phenomena observed in spin frustrated systems such as $CsNiCl_3$ and $CsCoCl_3$ [46]. Application of magnetic fields finally merges two transitions together at around 3 T. At higher field, the transition temperature has a dome-shaped boundary peaking at 5 T, as shown in Figure 16. Zero-field μSR spectra demonstrate a long-range magnetic order below T_{c2}, but a paramagnetic state for $T_{c2} < T < T_{c1}$ [45]. Thus, the transitions at T_{c1} and T_{c2} are, respectively, structural and magnetic.

The most prominent observation in $(CuBr)Sr_2Nb_3O_{10}$ is a 1/3 magnetization plateau in the magnetization curve (see Figure 17). The plateau becomes obscured with increasing T and vanishes at 9 K, in agreement with the phase boundary determined by heat capacity measurements. Since the magnetization curves at 4.2 K and 1.3 K are nearly identical, non-flat plateau is not due to thermal effects. Dzyaloshinskii-Moriya interactions and/or staggered g tensors are a possible origin as discussed in $SrCu_2(BO_3)_2$ [47].

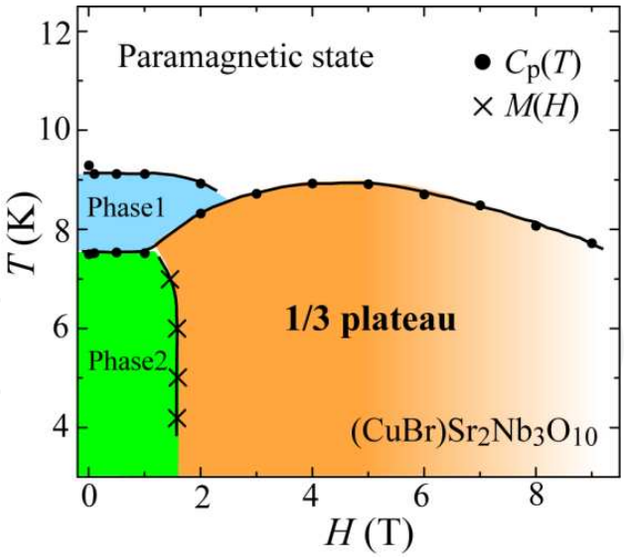

Figure 16. *T-H* phase diagram for $(CuBr)Sr_2Nb_3O_{10}$, determined by $C_p(T)$ and $M(H)$ [44].

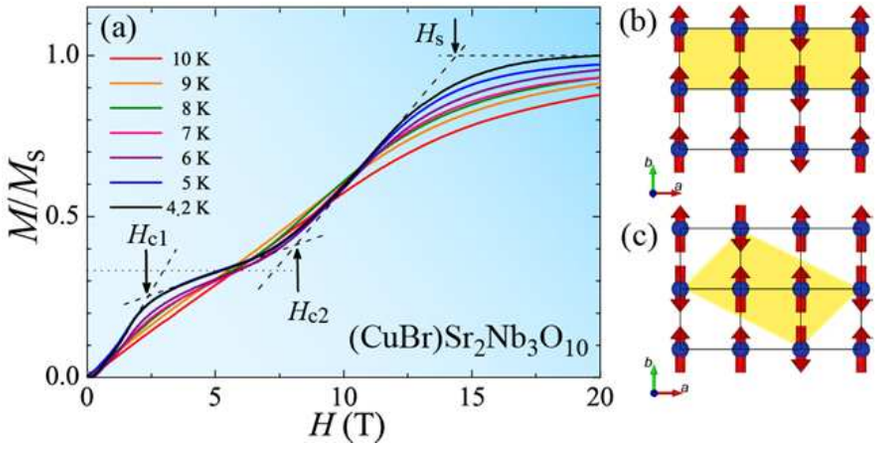

Figure 17. (a) High-field magnetization curves for $(CuBr)Sr_2Nb_3O_{10}$ [44]. (b, c) Originally proposed magnetic structures in the 1/3 plateau state. Only Cu ions are depicted. Magnetic unit cells are represented in yellow.

The 1/3 magnetization plateau has been theoretically predicted for various triangle-based lattices. Experimentally, triangular- and diamond-lattice antiferromagnets such as Cs_2CuBr_4 [48] and $Cu_3(CO_3)_2(OH)_2$ [49] exhibit the 1/3 plateau. However, for commensurability reasons, 1/2 and 1/4 plateaus are naturally expected for the square-based systems [50]. The exception is found in $SrCu_2(BO_3)_2$ with the Shastry-Sutherland lattice, which is due to the stronger 2nd NN interdimer interaction than the NN interdimer one [27]. Oshikawa *et al*. formulated the quantization condition [51]; $p(S - m)$ = integer, where p and m are the period of the spin state, the magnetization per site, respectively. For S = 1/2, the minimal necessary condition of the 1/3 plateau (m = 1/6) is p = 3. Since $(CuBr)Sr_2Nb_3O_{10}$ has one Cu^{2+} ion in its chemical unit cell (p = 1), the breaking of translational symmetry is needed to satisfy the quantization conditions. Based on these considerations, we initially proposed two possible in-plane magnetic structures with a propagation vector of (1/3 0) and (1/3 1/6) as shown in Figure 17(b) and 17(c), respectively [44].

In order to observe the magnetic structure at zero field and at the 1/3 plateau, the neutron powder diffraction experiments were carried out at ILL in Grenoble [52]. Figure 18 shows the magnetic diffraction patterns without magnetic field at 8 K and 2 K after subtraction of the 26 K nuclear data. The magnetic Bragg reflections were discernible below T_{c2}, while no magnetic reflections were detected above T_{c2}. The magnetic peaks can be indexed with the propagation vector of (0 3/8 1/2), and the magnetic structure is shown in Figure 19. The Cu moments rotate around the *c*-axis within the *ab* plane, and the helix propagates along the *b*-axis with a rotation of 135° between adjacent moments. The helical chains are coupled ferromagnetically along the *a*-axis. The ordered moment at 2 K is 0.79(7) μ_B/Cu^{2+}.

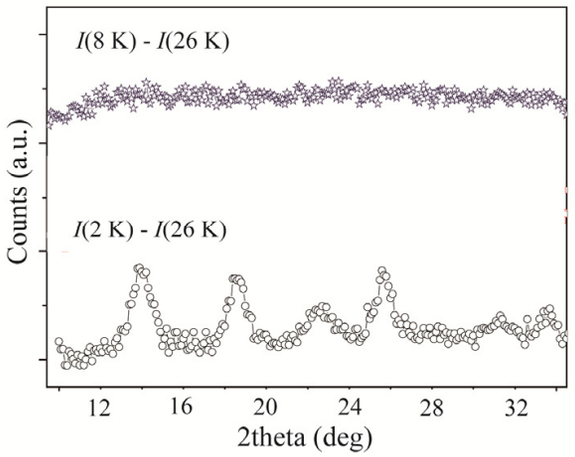

Figure 18. The low angle region of the magnetic diffraction patterns for (CuBr)$Sr_2Nb_3O_{10}$ at 8 and 2 K after subtraction of the 26 K nuclear pattern [52].

The observed helical AFM structure is incompatible with those expected from the simple J_1-J_2 model in the absence of magnetic field. It can only be explained when an additional magnetic interaction J_3 is introduced. In the J_1-J_2-J_3 model, several magnetically ordered states appear depending on J_1, J_2, J_3 [53-55]: (0 0) FM phase, (π π) NAF phase, (π 0) CAF phase, (0 q) spiral phase with $q = \cos^{-1}[-(J_1 + 2J_2)/4J_3]$, ($q$ q) spiral phase with $q = \cos^{-1}[-J_1/(2J_2 + 4J_3)]$. The propagation vector of (0 3/8) in (CuBr)$Sr_2Nb_3O_{10}$ corresponds to the third case. The magnetic Bragg reflections at 4.5 T (in the 1/3 plateaus region) can be indexed with an incommensurate propagation vector (0 1/3 0.446), which corresponds to the magnetic structure in Figure 17(c). Recently, Furukawa *et al*. have found theoretically helical AFM ordered states in the ferromagnetically coupled Shastry-Sutherland model [56]. Whether this model can explain the 1/3 plateau or not is interesting to check.

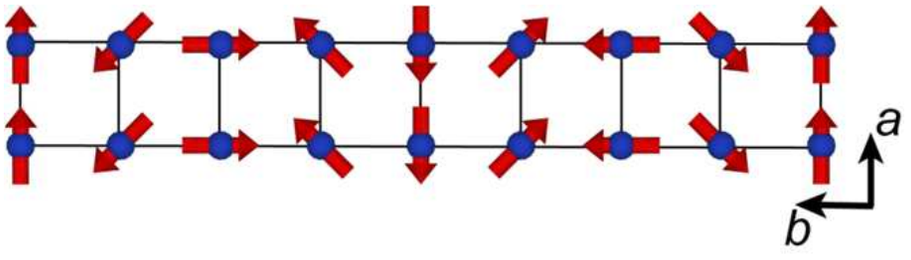

Figure 19. The magnetic structure of (CuBr)$Sr_2Nb_3O_{10}$ in zero field [52].

2.2.2. $(CuBr)A_2B_3O_{10}$ (A = Ca, Sr, Ba, Pb; B = Nb, Ta)

A series of triple layered copper bromides, $(CuBr)A_2B_3O_{10}$, was synthesized [45]. Since the Rb compounds could not be formed for A = Pb and Ba, $CsA_2B_3O_{10}$ was prepared as a precursor. $A'Pb_2Ta_3O_{10}$ (A' = Rb, Cs) could not be isolated because of formation of $Pb_3Ta_4O_{13}$ as a main phase. The ion-exchange reaction using $CuBr_2$ successfully proceeded at 320 – 350 °C. From the XRD patterns at room temperature, all the $(CuBr)A_2B_3O_{10}$ compounds are found to be isostructural with $(CuBr)Sr_2Nb_3O_{10}$. Both a- and c- axes show a linear increase with the ionic radius of A^{2+}, except Pb. A deviation from the linear relation for A = Pb is due to the steric effect of the $6s^2$ lone pair in Pb [57]. There is no B-site dependence because of the similar ionic radii.

The χ-T curves of $(CuBr)Ca_2B_3O_{10}$ exhibit a broad maximum. T_{max}, is 15 K for Nb and 22 K for Ta. The Weiss temperature θ is positive for all the compounds. $(CuBr)Ba_2Nb_3O_{10}$ shows a drastic drop at 5 K, suggesting an antiferromagnetic transition, while its Ta counterpart shows a monotonous temperature dependence, which is similar to that of $(CuBr)Sr_2Nb_3O_{10}$. Figure 20 shows the magnetizations normalized by the saturation magnetizations. The 1/3 plateau state is remarkably robust against the chemical substitution. As seen in Figure 20(c), $(CuBr)Pb_2Nb_3O_{10}$ exhibits a 1/3 plateau between H_{c1} = 1.7 T and H_{c2} = 5.8 T. The narrowed plateau region of the plateau (4.1 T) indicates that the A-site replacement by the larger cation destabilizes the plateau phase. Further increasing the size of the A-site cation leads to the disappearance of the plateau; no plateau was observed in $(CuBr)Ba_2Nb_3O_{10}$ (Figure 20(d)). Decreasing the size of the A-site (vs. Sr) produces the same results; no plateau was observed in $(CuBr)Ca_2Nb_3O_{10}$ (Figure 20(a)). As shown in Fig. 20(e), the $H_{c2} - H_{c1}$ vs. $r_A{}^{2+}$ plot clearly demonstrates an intimate correlation between $r_A{}^{2+}$ and the stability of the plateau phase.

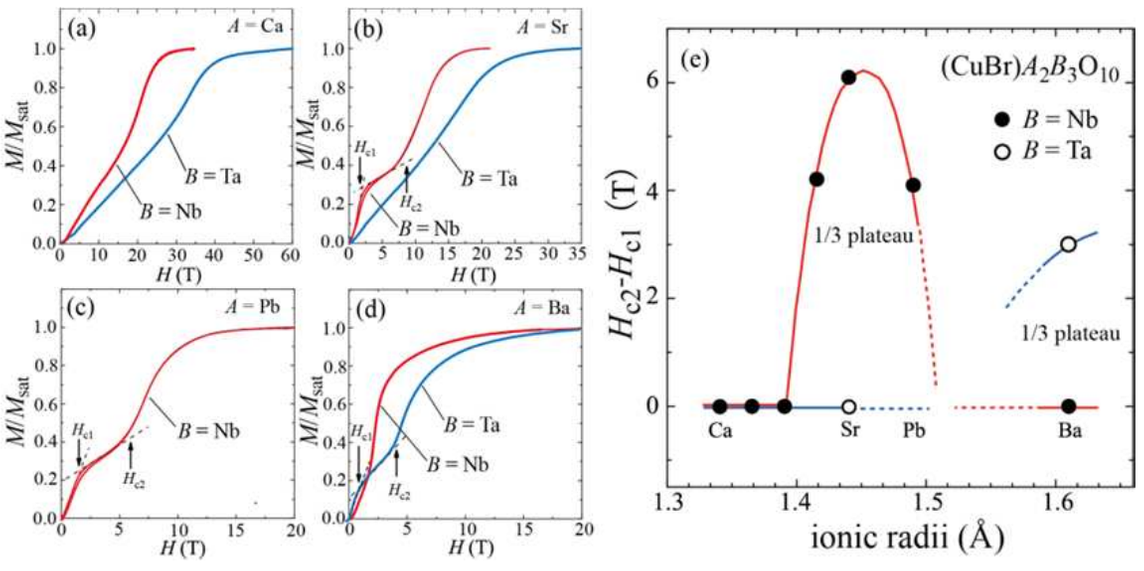

Figure 20. (a)-(d) Magnetization curves measured for $(CuBr)A_2B_3O_{10}$. (e) The compositional dependence of the plateau width $H_{c2} - H_{c1}$ as a function of the ionic radius of the A site [45].

The 1/3 plateau phase can be tuned not only by the *A* site but also by the *B* site. In the case of *B* = Ta, only (CuBr)$Ba_2Ta_3O_{10}$ showed a 1/3 plateau with H_{c1} = 1.0 T and H_{c2} = 4.0 T. Although the data available are limited, it is anticipated, in analogy to the Nb case, that the plateau-stabilizing region is shifted to the right in Figure 20(e). Conditions for the appearance of the plateau would come from a subtle balance between the magnetic interactions mediated by Br and those mediated by BO_6–BO_6.

2.3. Quadruple layered system

2.3.1. (CuCl)$Ca_2NaNb_4O_{13}$

A quadruple layered compound, (CuCl)$Ca_2NaNb_4O_{13}$ [58], was prepared by the reaction of $RbCa_2NaNb_4O_{13}$ [59] and $CuCl_2$ at 320 °C for 1 week. Laboratory XRD patterns of both $RbCa_2NaNb_4O_{13}$ and (CuCl)$Ca_2NaNb_4O_{13}$ at room temperature could be indexed in the tetragonal cell with the lattice parameters a = 3.869 Å and c = 18.859 Å, and a = 3.866 Å and c = 19.608 Å, respectively. The TEM and synchrotron powder diffraction experiments revealed superlattice reflections that are correlated with the original cell by $2a \times 2a \times c$ (Figure 21). Such a structural deviation from the ideal structure is reasonable in light of the tolerance factor ($t = [r_A + r_O]/\sqrt{2}[r_B + r_O]$). Perovskite compounds with the ideal cubic structure such as $SrTiO_3$ have t = 1. When t is smaller than unity, coherent octahedral tilting takes place. Indeed, t = 0.955 for (CuCl)$Ca_2NaNb_4O_{13}$, implying the octahedral tilting in the perovskite blocks. However, the precursor exhibited very weak and diffuse superlattice reflections. The difference in the TEM patterns would be related to the difference in the bonding nature connecting adjacent perovskite blocks; in $RbCa_2NaNb_4O_{13}$, the adjacent $Ca_2NaNb_4O_{13}$ blocks are weakly bound via the Rb cations, while in (CuCl)$Ca_2NaNb_4O_{13}$, the adjacent perovskite blocks are connected covalently via the edge-shared $CuCl_4O_2$ octahedra, which results in a long-ranged coherent octahedral tilting. In order to find the most reasonable space group for (CuCl)$Ca_2NaNb_4O_{13}$, Aleksandrov's analysis of symmetry reduction in response to octahedral tilting in layered perovskites was employed [60]. Among possible space groups, only *I*4/*mmm* with (++0) tilt met the extinction conditions derived from the TEM and XRD results. Here, + and 0 denote, respectively, in-phase tilt and no tilt in Glazer's notation [61].

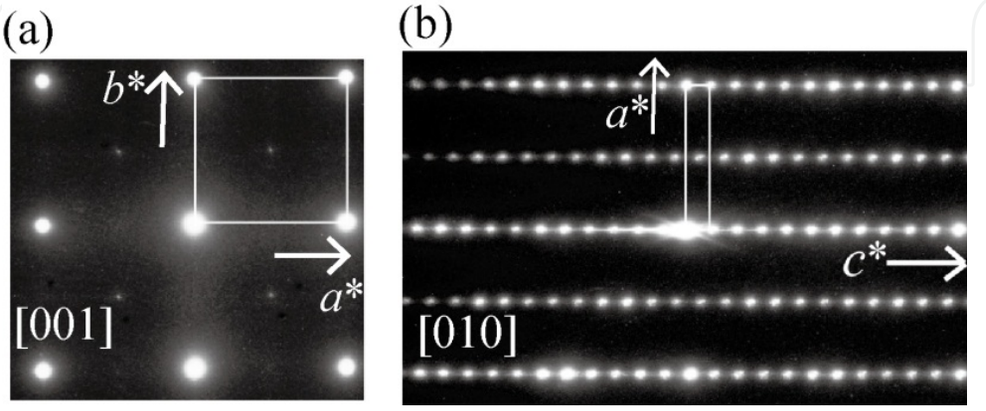

Figure 21. Electron diffraction patterns of (CuCl)$Ca_2NaNb_4O_{13}$ at room temperature obtained along the [001]- and [010]-zone axes [58].

The temperature dependence of magnetic susceptibility for $(CuCl)Ca_2NaNb_4O_{13}$ did not show an anomaly associated with magnetic ordering, which is also supported by μSR and specific heat measurements. FM interactions are dominant over AFM interactions, similar to the triple-layered CuBr compounds [45]. Figure 22 shows the magnetization curve measured at 1.3 K. The $M(H)$ does not show either a fractional magnetization plateau or other field-induced phase transitions, but a rather slow increase. The $M(H)$ does not saturate even at 57 T, implying that the in-plane interaction is fairly strong and that there is a strong competition between FM and AFM interactions.

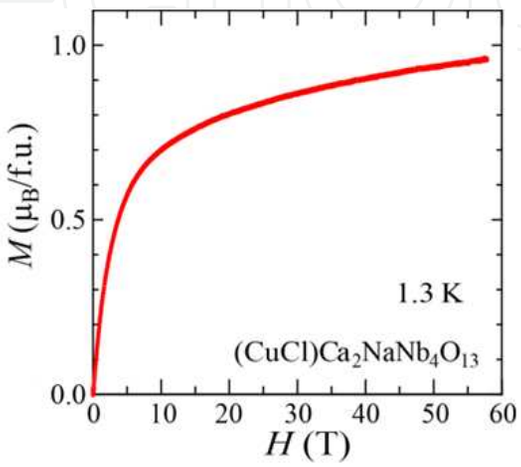

Figure 22. Magnetization curve of $(CuCl)Ca_2NaNb_4O_{13}$ at 1.3 K [58].

n	compounds	space group	magnetic features	T_N (K)	Δ/k_B (K)	θ (K)	Ref.
2	$(CuCl)LaNb_2O_7$	*Pbam* (2*a*×2*b*×*c*)	Spin-singlet state		26.7	–9.6	32
		*P*4/*mmm*					11
	$(CuCl_{1-x}Br_x)LaNb_2O_7$ ($0.05 \le x \le 1.0$)	*P*4/*mmm*	CAF order	7 (x = 0.05) 17 (x = 0.33) 21 (x = 0.50) 25 (x = 0.67) 32 (x = 1.0)		–	38, 39
	$(CuCl)La(Nb_{1-y}Ta_y)_2O_7$ ($0.2 \le y \le 1.0$)	*P*4/*mmm*	Coexistence of spin ordered and disordered states	7 ($0.2 \le y \le 0.9$)	23.2 (y = 0.2)	–5.6 (x = 0.20) –3.8 (x = 0.40) –3.1 (x = 0.60) –2.5 (x = 0.80)	39, 40
	$(CuCl)LaTa_2O_7$	*P*4/*mmm*	CAF order	7		–1.2	39, 40
3	$(CuBr)(Ca_{1-x}Sr_x)_2Nb_3O_{10}$ ($0 \le x \le 0.50$)	*P*4/*mmm*	AFM order	13 (x = 0)		4.6 (x = 0)	45
	$(CuBr)(Ca_{1-x}Sr_x)_2Nb_3O_{10}$ (x = 0.75, 1.0)	*P*4/*mmm*	Helical AFM order, 1/3 magnetization plateau	7.5 (x = 1.0)		20.9 (x = 1.0)	44, 45
	$(CuBr)Pb_2Nb_3O_{10}$	*P*4/*mmm*	AFM order, 1/3 magnetization plateau	~ 6		17.4	45
	$(CuBr)Ba_2Nb_3O_{10}$	*P*4/*mmm*	AFM order	5		14.9	45
	$(CuBr)Ca_2Ta_3O_{10}$	*P*4/*mmm*	AFM order	16.6		3.2	45
	$(CuBr)Sr_2Ta_3O_{10}$	*P*4/*mmm*	AFM order	11		13.2	45
	$(CuBr)Ba_2Ta_3O_{10}$	*P*4/*mmm*	AFM order, 1/3 magnetization plateau	5		14.7	45
4	$(CuCl)Ca_2NaNb_4O_{13}$	*I*4/*mmm* (2*a*×2*a*×*c*)	Paramagnetic state	–		22.4	58

Table 2. Space group, magnetic features, Neel temperature, T_N, spin-gap energy, Δ/k_B and Weiss temperature, θ for $(CuX)A_{n-1}B_nO_{3n+1}$ (X = Cl, Br; A = Na, La, Ca, Sr, Ba, Pb; B = Nb, Ta; n = 2, 3, and 4).

3. Conclusion

We have demonstrated that the ion-exchange reaction using the DJ phase that involves the simultaneous co-exchange of metal cations and halide anions is effective approach to design a new class of two-dimensional quantum spin antiferromagnets, with tuned in-plane magnetic interactions and a variety of quantum phases. A series of (CuX)$A_{n-1}B_nO_{3n+1}$ with the S = 1/2 square lattice exhibits novel quantum spin phenomena such as spin-liquid state, quantized magnetization plateau, quantum phase separation, and field-induced BEC state. They are caused by the strong competition between FM and AFM interactions. Table 2 summarizes the structural and magnetic properties in (CuX)$A_{n-1}B_nO_{3n+1}$. Note that most studies on spin frustrated magnetism has been focused so far on the systems composed of only AFM interactions. It is only recently that attentions have been paid to frustrated systems including FM interactions from both experimentally and theoretically points of view. We hope that the (CuX)$A_{n-1}B_nO_{3n+1}$ system will continue to contribute to the development of new physics of the frustrated spin systems in the future. The ion-exchange reaction can be extended to other compounds with transition metals with different spin quantum number, for example, (MCl)$LaNb_2O_7$ (M = Mn^{2+}, Fe^{2+}, etc.) [62–65] and (NiCl)$Sr_2Ta_3O_{10}$ [66]. Reflecting the classical nature of magnetic moment, (MCl)$LaNb_2O_7$ (M = Co, Fe, Mn) exhibit antiferromagnetic order, but several anomalous behaviors have been still observed due to geometrical frustration. The nickelic chloride with S = 1 undergoes the successive magnetic phase transitions with an intermediate phase characterized by a partial magnetic order. The advantage of the ion-exchange reactions is that, once one finds an appropriate precursor or hosts, any desired spin lattices can be constructed in principle. Using this topochemical strategy, various magnetic lattices (triangle, kagomé, pyrochlore, etc.) might be prepared.

Author details

Yoshihiro Tsujimoto
National Institute for Materials Science, Japan

Hiroshi Kageyama
Graduate School of Engineering, Kyoto University, Japan

Acknowledgement

The authors thank Prof. John B. Wiley, Prof. Yoshitami Ajiro, Prof. Kazuyoshi Yoshimura, Dr. Atsushi Kitada, Prof. Kazuma Hirota, Dr. Masakazu Nishi, Prof. Keisuke Totsuka, Prof. Masayuki Hagiwara, Prof. Yasuo Narumi, Prof. Koichi Kindo, Prof. Hiroi Zenji, Dr. Makoto Yoshida, Prof. Masashi Takigawa, Dr. Masaki Ichihara, Dr. Cédric Tassel, Prof. Yasutomo J. Uemura, Prof. Graeme M. Luke, Dr. Tatsuo Goko, Prof. Seung-Hun Lee, Prof. Bella Lake, Prof. Mike H. Whangbo, Prof. Werner Paulus, Dr. Olivier J. Hernandez, Dr. Clemens Ritter, Dr. Kunihiro Nakano, Prof. Yutaka Ueda, Dr. Sk Mohammad Yusuf, Prof. John P. Attfield, Dr. Tsutomu Momoi, Prof. Nic Shannon, and

Prof. Mikio Takano for their fruitful discussion and collaborations. This work was supported by the Japan Society for the Promotion of Science (JSPS) through its ''Funding Program for World–Leading Innovative R&D on Science and Technology (FIRST) Program", Grants-in-Aid for Science Research in the Priority Areas ''Novel States of Matter Induced by Frustration" (No. 19052004) and Grant-in-Aid for Scientific Research (A) (No. 22245009) from the Ministry of Education, Culture, Sports, Science and Technology of Japan, and CREST.

4. References

[1] Gopalakrishnan J. Chimie Douce Approaches to the Synthesis of Metastable Oxide Materials. Chem. Mater. 1995;7 1265-1275.

[2] Takada K, Sakurai H, Takayama-Muromachi E, Izumi F, Dilanian A, Sasaki T. Superconductivity in Two-Dimensional CoO_2 Layers. Nature 2003;422 53-55.

[3] Choy J-H, Kwon S-J, Park G-S. High T_c Superconductors in the Two-Dimensional Limit: $[(Py\text{-}C_nH_{2n+1})_2HgI_4]$-$BiSr_2Ca_{m-1}Cu_mOy$ (m = 1 and 2). Science 1998;280 1589-1592.

[4] Tsujimoto Y, Tassel C, Hayashi N, Watanabe T, Kageyama H, Yoshimura K, Takano M, Ceretti M, Ritter C, Paulus W. Infinite-Layer Iron Oxide with a Square-Planar Coordination. 2007;450 1062-1066.

[5] Schaak R, Mallouk T. E. Perovskites by Design: A Toolbox of Solid-State Reactions. Chem. Mater. 2002;14 1455-1471.

[6] Sanjaya Ranmohotti K. G, Josepha E, Choi J, Zhang J, Wiley J. B. Topochemical Manipulation of Perovskites: Low-Temperature Reaction Strategies for Directing Structure and Properties. Adv. Mater. 2011;23 442-460.

[7] Ebina Y, Sasaki T, Harada M, Watanabe M. Restacked Perovskite Nanosheets and Their Pt-loaded Materials as Photocatalysis. Chem. Mater. 2002;14 4390-4395.

[8] Machida M, Mitsuyama T, Ikeue K, Matsushima, S, Arai M. Photocatalytic Property and Electronic Structure of Triple-Layered Perovskite Tantalates, $MCa_2Ta_3O_{10}$ (M = Cs, Na, H, and $C_6H_{13}NH_3$). J. Phys. Chem. B 2005;109 7801-7806.

[9] Toda K, Watanabe J, Sato M. Synthesis and Ionic Conductivity of New Layered Perovskite Compound, $Ag_2La_2Ti_3O_{10}$. Solid State Ionics 1996;90 15-19.

[10] Nagai I, Abe Y, Kato M, Koike Y, Kakihana M. Synthesis and Superconducting Properties of Li-Intercalated Niobium Oxide $Li_xAB_2Nb_3O_{10}$. Solid State Ionics 2002;151 265-268.

[11] Kodenkandath T. A, Lalena J. N, Zhou W. L, Capenter E. E, Sangregorio C, Falster A. U, Simmons W. B, O'Connor C. J, Wiley J. B. Assembly of Metal-Anion Arrays within a Perovskite Host. Low-Temperature Synthesis of New Layered Copper-Oxyhalides, $(CuX)LaNb_2O_7$, X = Cl, Br. J. Am. Chem. Soc. 1999;121 10743-10746.

[12] Kodenkandath T. A, Kumbhar A, Zhou W. L, Wiley J. B. Construction of Copper Halide Networks within Layered Perovskites. Synthesis and Characterization of New-Temperature Copper Oxyhalides. Inorg. Chem. 2001;40 710-714.

[13] Anderson P. W. The Resonating Valence Bond state in La_2CuO_4 and Superconductivity. Science 2012;235 1196-1198.

[14] Read N, Sachdev S. Valence-Bond and Spin-Peierls Ground States of Low-Dimensional Quantum Antiferromagnets. Phys. Rev. Lett. 1989;62 1694-1697.

[15] Gelfand M, Singh R. R. P, Huse D. A. Zero-Temperature Ordering in Two-Dimensional Frustrated Quantum Heisenberg Antiferromagnets. Phys. Rev. B 1989;40 10801-10809.

[16] Becca F, Mila F. Peiers-Like Transition Induced by Frustration in a Two-Dimensional Antiferromagnet. Phys. Rev. Lett. 2002;89 037204-1-4.

[17] Shannon N, Schmidt B, Penc K, Thalmeier P. Finite Temperature Properties and Frustrated Ferromagnetism in a Square Lattice Heisenberg Model. Eur. Phys. J. B 2004;38 599-616.

[18] Shannon N, Momoi T, Sindzingre P. Nematic Order in Square Lattice Frustrated Ferromagnets. Phys. Rev. Lett. 2006;96 027213-1-4.

[19] Melzi R, Carretta P, Lascialfari A, Mambrini M, Troyer M, Millet P, Mila F. $Li_2VO(Si, Ge)O_4$, a Prototype of a Two-Dimensional Frustrated Quantum Heisenberg Antiferromaget. Phys. Rev. Lett. 2000;85 1318-1321.

[20] Nath R, Furukawa Y, Borsa F, Kaul E. E, Baenitz M, Geibel C, Johnston D. C. Single-Crystal ^{31}P NMR Studies of the Frustrated Square-Lattice Compound $Pb_2VO(PO_4)_2$. Phys. Rev. B 2009;80 214430-1-10.

[21] Kageyama H, Kitano T, Oba N, Nishi M, Nagai S, Hirota K, Viciu L, Wiley J. B, Yasuda J, Baba Y, Ajiro Y, Yoshimura K. Spin-Singlet Ground State in Two-Dimensional S = 1/2 Frustrated Square Lattice: $(CuCl)LaNb_2O_7$. J. Phys. Soc. Jpn. 2005;74 1702-1705.

[22] Caruntu G, Kodenkandath T. A, Wiley J. B. Neutron Diffraction Study of the Oxychloride Layered Perovskite, $(CuCl)LaNb_2O_7$. Mat. Res. Bull. 2002;37 593-598.

[23] Zheludev A, Shirane G, Sasago Y, Hase M, Uchinokura K. Dimerized Ground State and Magnetic Excitations in $CaCuGe_2O_6$. Phys. Rev. B 1996;53 11642-11646.

[24] Kageyama H, Nishi M, Aso N, Onizuka K, Yoshihama T, Nukui K, Kodama K, Kakurai K, Ueda Y. Direct Evidence for the Localized Single-Triplet Excitations and the Dispersive Multitriplet Excitations in $SrCu_2(BO_3)_2$. Phys. Rev. Lett. 2000;84 5876-5879.

[25] Kageyama H, Yasuda J, Kitano T, Totsuka K, Narumi Y, Hagiwara M, Kindo K, Baba Y, Ajiro Y, Yoshimura K. Anomalous Magnetization of Two-Dimensional S = 1/2 Frustrated Square-Lattice Antiferromagnet $(CuCl)LaNb_2O_7$. J. Phys. Soc. Jpn. 2005;74 3155-3158

[26] Kageyama H, Yoshimura K, Stern R, Mushnikov N. V, Onizuka K, Kato M, Kosuge K, Slichter C. P, Goto T, Ueda Y. Exact Dimer Ground State and Quantized Magnetization Plateaus in the Two-Dimensional Spin Sytem $SrCu_2(BO_3)_2$. Phys. Rev. Lett. 1999;82 3168-3171.

[27] Onizuka K, Kageyama H, Narumi Y, Kindo K, Ueda Y, Goto T. 1/3 Magnetization Plateau in $SrCu_2(BO_3)_2$ - Stripe Order of Excited Triplets -. J. Phys. Soc. Jpn. 2000;64 1016-1018.

[28] Shiramura W, Takatsu K, Kurniawan B, Tanaka H, Uekusa H, Ohashi Y, Takizawa K, Mitamura H, Goto T. Magnetization Plateaus in NH_4CuCl_3. J. Phys. Soc. Jpn. 1998;67 1548-1551.

[29] Kitada A, Hiroi Z, Tsujimoto Y. Kitano T, Kageyama H, Ajiro Y, Yoshimura K. Bose-Einstein Condensation of Quasi-Two-Dimensional Frustrated Quantum Magnet (CuCl)$LaNb_2O_7$. J. Phys. Soc. Jpn. 2007;76 093706-1-4.

[30] Nikuni T, Oshikawa M, Oosawa A, Tanaka H. Bose-Einstein Condensation of Dilute Magnons in $TlCuCl_3$. Phys. Rev. Lett. 2000;84 5868-5871.

[31] Yoshida M, Ogata N, Takigawa M, Yamaura J, Ichihara M, Kitano T, Kageyama H, Ajiro Y, Yoshimura K. Magnetic and Structural Studies of the Quasi-Two-Dimensional Spin-Gap System (CuCl)$LaNb_2O_7$. J. Phys. Soc. Jpn. 2007;76 104703-1-9.

[32] Tassel C, Kang J, Lee C, Hernandez O, Qiu Y, Paulus W, Collet E, Lake B, Guidi T, Whangbo M.-H, Ritter C, Kageyama H, Lee S.-H. Ferromagnetically Coupled Shastry-Sutherland Quantum Spin Singlets in (CuCl)$LaNb_2O_7$. Phys. Rev. Lett. 2010;105 167205-1-4.

[33] Hernandez O. J, Tassel C, Nakano K, Paulus W, Ritter C, Collet E, Kitada A, Yoshimura K, Kageyama H. First Single-Crystal Synthesis and Low-Temperature Structural Determination of the Quasi-2D Quantum Spin Compound (CuCl)$LaNb_2O_7$. Dalton Trans. 2011;40 4605-4613.

[34] Kumada N, Kinomura N, Sleight A. W. $CsLaNb_2O_7$, Acta Crystallogr., Sect. C: Cryst. Struct. Commun. 1996;C52 1063-1065.

[35] Shastry B. S, Sutherland B. Exact Ground State of a Quantum Mechanical Antiferromagnet. Physica B 1981;108 1069-1070.

[36] Yoshida M, Ogata N, Takigawa M, Kitano T, Kageyama H, Ajiro Y, Yoshimura K. Antiferromagnetic Nuclear Resonance in the Quasi-Two-Dimensional (CuBr)$LaNb_2O_7$. J. Phys. Soc. Jpn. 2008;77 104705-1-7.

[37] Oba N, Kageyama H, Kitano T, Yasuda J, Baba Y, Nishi M, Hirota K, Narumi Y, Hagiwara M, Kindo K, Saito T, Ajiro Y, Yoshimura K. Collinear Order in Frustrated Quantum Antiferromagnet on Square Lattice (CuBr)$LaNb_2O_7$. J. Phys. Soc. Jpn. 2006;75 113601-1-4.

[38] Tsujimoto Y, Kitada A, Kageyama H, Nishi M, Narumi Y, Kindo K, Kiuchi Y, Ueda Y, Uemura Y. J, Ajiro Y, Yoshimura K. Synthesis Structural and Magnetic Properties of the Soild Solution $(CuCl_{1-x}Br_x)LaNb_2O_7$. J. Phys. Soc. Jpn. 2010;79 014709-1-4.

[39] Uemura Y. J, Aczel A. A, Ajiro. Y, Carlo J. P, Goko T, Goldfield D. A, Kitada A, Luku G. M, MacDougall G. J, Mihailescu I. G, Rodriquez J. A, Russo P. L, Tsujimoto Y, Wiebe C. R, Williams T. J, Yamamoto T, Yoshimura K, Kageyama H. Muon Spin Relaxation of the Frustrated Quasi-Two-Dimensional Square-Lattice Spin System Cu(Cl, Br)La(Nb,

Ta)$_2$O$_7$: Evolution From Spin-Gap to Antiferromagnetic State. Phys. Rev. B 2009;80 174408-1-9.

[40] Kitada A, Tsujimoto Y, Kageyama H, Ajiro Y, Nishi M, Narumi Y, Kindo K, Ichihara M, Ueda Y, Uemura Y. J, Yoshimura K. Quantum Phase Transition in (CuCl)La(Nb$_{1-x}$Ta$_x$)$_2$O$_7$. Phys. Rev. B 2009;80 174409-1-5.

[41] Uemura Y. J, Yamazaki T, Harshman D. R, Senba M, Ansaldo E. J. Muon-Spin Relaxation in AuFe and CuMn Spin Glasses. Phys. Rev. B 1985;31 546-563.

[42] Kojima K. M, Fudamoto Y, Larkin M, Luke G. M, Merrin J, Nachumi B, Uemura Y. J, Hase M, Sasago Y, Uchinokura K, Ajiro Y, Revcolevschi A, Renard J. P. Antiferromagnetic Order with Spatially Inhomogeneous Ordered Moment Size of Zn- and Si-Doped CuGeO$_3$. Phys. Rev. Lett. 1997;79 503-506.

[43] Ohsugi S, Tokunaga Y, Ishida K, Kitaoka Y, Azuma M, Fujishiro Y, Takano M. Impurity-Induced Staggered Polarization and Antiferromagnetic Order in Spin-1/2 Heisenberg Two-Leg Ladder Compound SrCu$_2$O$_3$: Extensive Cu NMR and NQR Studies. Phys. Rev. B 1999;60 4181-4190.

[44] Tsujimoto Y, Baba Y, Oba N, Kageyama H, Fukui T, Narumi Y, Kindo K, Saito T, Takano M, Ajiro Y, Yoshimura K. 1/3 Magnetization Plateau in Spin-1/2 Square Lattice Antiferromagnet (CuBr)Sr$_2$Nb$_3$O$_{10}$. J. Phys. Soc. Jpn. 2007;76 063711-1-4.

[45] Tsujimoto Y, Kageyama H, Baba Y, Kitada A, Yamamoto T, Narumi Y, Kindo K, Nishi M, Carlo J. P, Aczel A. A, Williams T. J, Goko T, Luke G. M, Uemura Y. J, Ueda Y, Yoshimura K. Synthesis Structure and Magnetic Properties of the Two-Dimensional Quantum Antiferromagnets (CuBr)A_2B_3O$_{10}$ (A = Ca, Sr, Ba, Pb; B = Nb, Ta) with the 1/3 Magnetization Plateau. Phys. Rev. B 2008;78 214410-1-10.

[46] Collins M. F, Petrenko O. A. Triangular Antiferromagnets. Can. J. Phys. 1997;75 605-655.

[47] Kodama K, Miyahara S, Takigawa M, Horvatic M, Berthier C, Mila F, Kageyama H, Ueda Y. Field-Induced Effects of Anisotropic Magnetic Interactions in SrCu$_2$(BO$_3$)$_2$. J. Phys.: Condens. Matter 2005;17 L61-L68.

[48] Ono T, Tanaka H, Aruga Katori H, Ishikawa F, Mitamura H, Goto T. Magnetization Plateau in the Frustrated Quantum Spin System Cs$_2$CuBr$_4$. Phys. Rev. B 2003;67 104431-1-7.

[49] Kikuchi H, Fujii Y, Chiba M, Mitsudo S, Idehara T, Tonegawa T, Okamoto K, Sakai T, Kuwai T, Ohta H. Experimental Observation of the 1/3 Magnetization Plateau in the Diamond-Chain Compound Cu$_3$(CO$_3$)$_2$(OH)$_2$. Phys. Rev. Lett. 2005;94 227201-1-4.

[50] Honecker A. Lanczos Study of the S = 1/2 Frustrated Square-Lattice Antiferromagnet in a Magnetic Field. Can. J. Phys. 2001;79 1557-1563.

[51] Oshikawa M, Yamanaka M, Affleck I. Magnetization Plateaus in Spin Chains: ''Haldane Gap'' for Half-Integer Spins. Phys. Rev. Lett. 1997;78 1984-1987.

[52] Yusuf S. M, Bera A. K, Ritter C, Tsujimoto Y, Ajiro Y, Kageyama H, Attfield J. P. Magnetic Correlation in the Square-Lattice Spin System (CuBr)$Sr_2Nb_3O_{10}$: A Neutron Diffraction Study. Phys. Rev. B 2011;84 064407-1-6.

[53] Feldner, H, Cabra D. C, Rossini G. L. Ferromagnetic Frustrated Spin Systems on the Square Lattice: Schwinger Boson Study. Phys. Rev. B 2011;84 214406-1-7.

[54] Sindzingre P. Spin-1/2 Frustrated Antiferromagnet on a Spatially Anisotropic Square Lattice Contribution of Exact Diagonalization. Phys. Rev. B 2004;69 094418-1-14.

[55] Sindzingre P, Seabra L, Shannon, Momoi T. Phase Diagram of the Spin-1/2 J_1-J_2-J_3 Heisenberg Model on the Square Lattice with Ferromagnetic J_1. J. Phys.: Conf. Ser. 2009;145 012048-1-6.

[56] Furukawa S, Dodds T, Kim Y. B. Ferromagnetically Coupled Dimers on the Distorted Shastry-Sutherland Lattice: Application to (CuCl)$LaNb_2O_7$. Phys. Rev. B 2011;84 054432-1-19.

[57] Belik A. A, Azuma M, Saito T, Shimakawa Y, Takano M. Crystallographic Features and Tetragonal Phase Stability of $PbVO_3$, a New Member of $PbTiO_3$ Family. Chem. Mater. 2005;17 269-273.

[58] Kitada A, Tsujimoto Y, Yamamoto T, Kobayashi Y, Narumi Y, Kindo K, Aczel A. A, Luke G. M, Uemura Y. J, Kiuchi Y, Ueda Y, Yoshimura K, Ajiro Y, Kageyama H. Quadruple-Layered Perovskite (CuCl)$Ca_2NaNb_4O_{13}$. J. Solid State Chem. 2012;185 10-17.

[59] Sugimoto W, Ohkawa H, Naito M, Sugawara Y, Kuroda K. Synthesis and Structures of Reduced Niobates with Four Perovskite-like Layers and Their Semiconducting Properties. J. Solid State Chem. 1999;148 508-512.

[60] Aleksandrov K. S. Structural Phase Transitions in Layered Perovskitelike Crystals. Crystallography Reports 1995;40 251-272.

[61] Glazer A. M. The Classification of Tilted Octahedra in Pervskites. Acta Crystallogr. B 1972;28 3384-3392.

[62] Viciu L, Caruntu G, Royant N, Koenig J, Zhou W. L, Kodenkandath T. A, Wiley J. B. Formation of Metal-Anion Arrays within Layered Perovsktie Hosts. Preparation of a Series of New Metastable Transition-Metal Oxyhalides, (MCl)$LaNb_2O_7$ (M = Cr, Mn, Fe, Co). Inorg. Chem. 2002;41 3385-3388.

[63] Viciu L, Golub V. O, Wiley J. B. Structural, Thermal and Magnetic Characterization of the Manganese Oxyhalide Layered Perovskite, (MnCl)$LaNb_2O_7$. J. Solid State Chem. 2003;175 88-93.

[64] Viciu L, Koenig J, Spinu L, Zhou W. L, Wiely J. B. Insertion of a Two-Dimensional Iron-Chloride Network between Perovskite Blocks. Synthesis and Characterization of the Layered Oxyhalide, (FeCl)$LaNb_2O_7$. Chem. Mater. 2003;15 1480-1485.

[65] Kitada A, Tsujimoto Y, Yajima T, Yoshimura K, Ajiro Y, Kobayashi Y, Kageyama H. Two-dimensional Frustrated Antiferromagnets (MCl)$LaNb_2O_7$ (M = Mn, Co, Cr). J. Phys.: Conf. Series 2011;320 012035-1-6.

[66] Tsujimoto Y, Kitada A, Uemura Y. J, Goko T, Aczel A. A, Williams T. J, Luke G. M, Narumi Y, Kindo K, Nishi M, Ajiro Y, Yoshimura K, Kageyama H. Two-Dimensional *S* = 1 Quantum Antiferromagnet (NiCl)$Sr_2Ta_3O_{10}$. Chem. Mater. 2010;22 4625-4631.

IntechOpen